

Degradation Differences of a Single Proton Exchange Membrane Fuel Cell: Energy Management Strategy and Dynamic Programming

*Lihang Han, Rui Lin**, Di Zhong, Hang Yu, Shenghao Tang

School of Automotive Studies, Tongji University, Shanghai 201804, China

*E-mail: ruilin@tongji.edu.cn

Received: 14 October 2020 / *Accepted:* 23 December 2020 / *Published:* 31 January 2021

The durability of proton exchange membrane fuel cells (PEMFC) is one of the limitations to its wide application in vehicles and other equipment. In this paper, a running profile of PEMFC using dynamic programming (DP) energy management strategy (EMS) is designed. The degradation of a single PEMFC is studied by running a single PEMFC under the designed cycle. Voltage decline rate reaches 1240 $\mu\text{V/h}$ at 600 $\text{mA/cm}^2/\text{s}$, faster than most Acceleration Stress Tests (AST). Performance decline difference in different areas of a single PEMFC is investigated. Degradation differences in 6 regions are analyzed using Localized Electrochemical Impedance Spectroscopy (EIS). The results show that the gas inlet area has higher and increasing high frequency resistance (HFR). Degradation of proton transport of proton exchange membrane (PEM) is related to hydrogen concentration and water content in the membrane. Gas inlet regions are less affected by mass transfer. This may due to less water being produced and accumulated near the gas inlet. Deterioration of mass transfer is related to corrosion of reactants/products micro channels that damage drainage capacity. Accumulated water blocks the transportation of reactants and causes flooding phenomenon. Charge transfer resistance also increases, indicating that catalyst layers also suffer during the durability experiments.

Keywords: PEMFC; Durability; Localized EIS; DP; EMS

1. INTRODUCTION

Proton exchange membrane fuel cell (PEMFC) is regarded as one of the most promising electricity generation technology[1,2]. It doesn't generate pollutants during operation, and its efficiency is not limited to the Carnot Cycle, which provides the upper-efficiency limit of the Internal Combustion Engines (ICE). As people become more aware of the importance of energy conservation and environmental protection[3], PEMFC is becoming a promising replacement of the traditional vehicle engine.

However, PEMFC cannot be widely applied as the vehicle engine until its durability is solved. PEMFC's performance could rapidly decrease when operated under unsteady power demand. Researches showed that the voltage degradation rate of PEMFC reached 110 $\mu\text{V}/\text{h}$ under potential cycling from 0.4 to 0.95[4], while stationary PEMFC only had the performance degradation of 3–6 $\mu\text{V}/\text{h}$ at 400 mA/cm^2 [5,6]. PEMFC engine used in the vehicle put forward even higher requirements to fuel cells durability. As the speed of a vehicle could change irregularly, the power of the PEMFC engine changes accordingly. Although other affiliate energy storage equipment, such as Lithium-ion battery, could help provide part of the power, the PEMFC engine's power variates according to the vehicle's needed power anyway.

PEMFC engine's durability is highly affected by the following operating conditions: idle running, load variation, overload, start-stop, cold-start. Many researchers studied the durability and performance decline of the PEMFC under these conditions. R. Lin[7] used a dynamic driving cycle, which included idle, full load, variable load, constant load running conditions, to investigate performance degradation. PEMFC's decline rate reached 1.7mA/cycle at 0.8 V. Current density distribution, EIS, CV, Scanning Electron Microscopy (SEM) methods were used to analyze its degradation characteristics. N. Zhao[8] conducted Open Circuit Voltage (OCV) accelerate stress test (AST) to study the effects of PEMFC's temperature and gas relative humidity on membrane durability. Zhang et al. completed a 94 h high-current aging of the fuel cell[9]. The open-circuit potential (OCV) of the PEMFC dropped from 0.95 V to 0.85 V, and the voltage at a current density of 400 mA/cm^2 reduced from 0.77 V to 0.70 V. J Han [10] investigated the durability of a PEMFC stack using the NEDC load profile under different operating temperatures. The degradation of the voltage was more at high temperature than low temperature. PEMFC's cold start performance of different flow fields had been researched, and the single serpentine flow field had good cold-start performance[11]. Mayur [12,13] used degradation models to study the performance degradation of PEMFC during vehicle driving cycles such as NEDC and WLTC. The transient performance of PEMFC after NEDC profile was investigated by the Computational Fluid Dynamics (CFD) method [14].

PEMFC engine has a slow power response and should be run in a suitable range as much as possible to maximize the fuel cell's life[15]. Besides, PEMFC cannot store energy. In combination with an energy storage system such as a battery, the fuel cell vehicle (FCV) can be driven by the two power sources together, which can reduce the change rate of power of the fuel cell. The excess power can also be stored. In a FCV, energy management strategy (EMS) splits the required power and allocates power between the fuel cell engine and the energy storage system. The EMS can control the dynamic behavior of FCV, thereby affecting system efficiency, hydrogen consumption, and FCV's life [16]. Energy management strategies are divided into two categories: rule-based strategy and optimization-based strategy [17]. The rule-based strategy can be subdivided into thermostat control strategy, power follow strategy, fuzzy control, etc. This type of strategy runs according to the preset rules. The optimization-based control strategy considers the target indicators, such as equivalent hydrogen consumption, lifespan, to achieve the optimal power distribution strategy. It can be further divided into global optimization strategies and real-time optimization strategies. Dynamic Programming (DP) belongs to the global optimization strategy and is widely studied [18,19]. The equivalent consumption minimization strategy can be applied to real-time control [20].

Although EMS of FCVs was widely studied. There was not much research on the actual performance of PEMFC under these designed EMS, especially for the optimization-based strategy, such as DP. What is the performance of PEMFC, and how does the PEMFC decline using designed EMS hasn't been studied in detail yet. PEMFC usually has a larger active area. Due to the difference in external conditions and internal structure, different areas' performance and deterioration rates are different. Therefore, it is necessary to study the degradation mechanism in different regions. Various methods can be used to investigate the performance degradation. Current density distribution can show differences in PEMFC performance but cannot provide more information. Electrochemical impedance spectroscopy (EIS) has the ability to separate electrochemical processes with different time constants and explore the reaction mechanism deeply. Traditional EIS test applies AC signals to the whole single cell, which cannot characterize the performance difference between different areas of PEMFC. The Localized Electrochemical Impedance Spectroscopy (Local EIS) is one method to provide information on different areas by measuring the impedance spectrum of a specific area in a PEMFC [21]. It can be used to characterize fuel cell degradation mechanisms and analyze the causes of local performance differences. This article uses the Localized EIS method to measure different areas' impedance spectra (Seg 1-6). Thus the electrochemical reaction phenomena in different regions and the differences in the mechanism of degradation can be analyzed. At present, relatively few studies explore the durability of PEMFCs using localized EIS. In this paper, the same local EIS technology as Liu [21] was used in the durability test. Other methods, like the single cell's EIS and polarization curve, were also discussed.

This paper studied PEMFC's degradation under dynamic programming energy management strategy. The paper consisted of two parts. In the first part, Worldwide harmonized Light vehicles Test Cycles (WLTC) was chosen as the driving cycle. Dynamic programming (DP) EMS was used to design the split of power to get the PEMFC engine's running profile. In the second part, a 50 cm² single PFMFC was used and operated under the designed profile for 100 cycles. Performance and degradation mechanisms were studied using Localized EIS. Results showed that high frequency resistance changes were related to hydrogen concentration and water content in the membrane. Proton transfer ability declined at high hydrogen concentration areas as hydrogen might cause Pt reduction and deposition at the PEM. Fully hydrated membrane provided good proton transfer circumstance and could help alleviate degradation of PEM. Charge transfer resistance increased from 1.46 to 2.05 mΩ. This was because the designed cycle caused the loss of Pt, which inevitably led to the loss of electrochemical surface area (ECSA), and irreversibly reduced the performance of PEMFC. Corrosion of carbon support and ionomer at catalyst layers could also decrease the number of reaction sites. The mass transfer was related to the flooding phenomenon. The drainage capacity decreased, which caused the flooding phenomenon to become more serious during the experiments. Gas inlet suffered less from the mass transfer. It could be attributed to less water produced and accumulated near the gas inlet area.

2. EXPERIMENTAL PART

2.1. PEMFC running profile using Dynamic Programming

Dynamic programming (DP) can solve the optimal control problem of a nonlinear system. The solution idea is to decompose the problem into smaller sub-problems. By discretizing time, State of

Charge (SOC) of the battery, and fuel cell power, the energy management strategy that minimizes hydrogen consumption in a driving cycle can be solved.

PEMFC stack model is built using experimental data of a single cell. PEMFC stack model is composed of 270 cells with an active area of 200 cm². When the fuel cell starts to work, power of the stack should be in the range of 13-52 kW. Single cell's voltage is in 0.6-0.8 V. When PEMFC stack works in the low current density, efficiency of PEMFC engine is low when considering auxiliary systems such as DC/DC converter [22]. The efficiency curve can be calculated using Eq. (1). V is the voltage of single cell. ΔH is the reaction heat. F is the Faraday's constant. η_{DC} is DC/DC converter's efficiency. η_{aux} is the efficiency of other auxiliary systems.

$$\eta_{fc} = \frac{V}{\Delta H \cdot 2F} \eta_{DC} \eta_{aux} \quad (1)$$

Lithium-ion battery model has a normal voltage of 400 V, with internal resistance r of 0.2 Ω . Open circuit voltage V_O is 465.6 V. Capacity of the battery C is 20 A·h, which can provide the energy needed to drive the car for an hour at ~110 km/h. State of Charge (SOC) of the battery can be calculated using Eq. (2). Battery's current I_b is calculated using Eq. (3). P_b is the power of the battery.

$$SOC_t = SOC_0 - \frac{1}{C} \int_0^t I_b dt \quad (2)$$

$$I_b = \frac{V_O - \sqrt{V_O^2 - 4P_b r}}{2r} \quad (3)$$

Power demand for fuel cell vehicle can be calculated using Eq. (1). Vehicle parameters are list in Table 1. Mass m is set to 1848 kg. Resistance coefficient f is 0.01. Correction coefficient of rotating mass δ is 1.1. Drag coefficient C_D is 0.29. Transmission ratio i_0 is 3.478. The wheel radius r is 0.334 m. Slope gradient i was set to 0. Transmission efficiency η is set to 0.9. And g is 9.8 m/s². u represents vehicle speed. T_m is the torque the motor has to provide. WLTC is designed based on the real-world driving data of different regions of the world [27], which can represent the vehicle's driving condition well. Speed and acceleration values of WLTC are put into Eq. (4) to obtain the required vehicle power, which is shown in Fig. 1.

$$\frac{T_m i_0 \eta}{r} = mgf + \frac{C_D A}{21.15} u^2 + mgi + \delta m \frac{du}{dt} \quad (4)$$

Table 1. Parameters used in the fuel cell vehicle.

Parameters	m (kg)	A (m ²)	r (m)	i	f	C_D
Value	1848	2.55	0.334	3.478	0.01	0.29
Parameters	δ	η	V_{norm} (V)	n_{fc}	A_{fc} (cm ²)	g (m/s ²)
Value	1.1	0.9	400	270	200	9.8

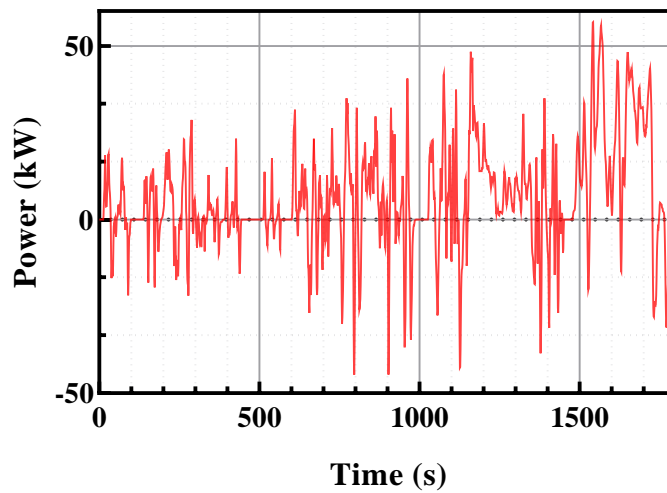


Figure 1. Power demand of FCV under WLTC

WLTC time is half an hour. To design DP energy management strategy (EMS) under WLTC, the time is discretized in 1 s interval. The whole working condition is divided into 1800 stages ($k = 1, 2, \dots, 1800$). State of DP algorithm used in this paper is SOC of battery. The SOC is discretized with a precision of 0.0001. SOC is in the range of 0.4-0.8. In the entire driving cycle, the required vehicle power should be provided solely by PEMFC. Therefore, SOC at the end of the driving cycle should be the same as the initial value. The permitted SOC values at different stages are expressed in Eq. (5).

$$SOC = \begin{cases} 0.4 + 0.0001i, i = 0, \dots, 4000, k = 2, \dots, 1799 \\ 0.6 & k = 1, 1800 \end{cases} \quad (5)$$

$$SOC_{k+1} = SOC_k - \frac{V_O - \sqrt{V_O^2 - 4(P_{v,k} - P_{b,k})r}}{2rC_b} \quad (6)$$

$$v_k = \frac{SMNI}{2000F} + \frac{I_b U_b}{1.2 \times 10^8 \eta_{avg}} \quad (7)$$

$$\begin{cases} f_{1801}(SOC_{1801}) = 0 \\ f_k(SOC_k) = \min\{v_k + f_{k+1}(SOC_{k+1})\}, k = 1800, \dots, 1 \end{cases} \quad (8)$$

PEMFC engine's power is the decision in the DP algorithm. The PEMFC power is divided at 1 kW precision ($P_{fc} = 0, 1, \dots, 52$ kW). State transfer equation is expressed in Eq. (6), which shows how SOC changes with decisions. The objective function is Eq. (7). This function converts the electric energy consumed or absorbed by the Lithium-ion battery into the corresponding hydrogen consumption and adds it with the fuel cell engine's hydrogen consumption to obtain the equivalent hydrogen consumption. v_k is the hydrogen consumption rate (kg/s) at stage k ; hydrogen Stoichiometry S is 1.5; Molar Mass of hydrogen M is 2 g/mol; N is the number of cells, which is 270; Faraday's constant F is 96485 C/mol. η_{avg} is the average efficiency of PEMFC. Apart from the equations discussed above, the fuel cell engine does not provide power when the vehicle's required power is or below zero. PEMFC engine's power is in the range of 13-52 kW when FCV's required power is above zero. And power change rate of PEMFC is limited to 2 kW/s. Besides, the efficiency of the power train is set as 0.9.

DP algorithm solves the energy management problem using Eq. (8). It solves the problem from stage 1800 to stage 0. The higher the discrete accuracy, the more accurate the calculation result. Fig. 2a)

shows the PEMFC engine’s power-time curve under DP EMS. Fig. 2b) shows a histogram of power. It could be seen that fuel cell fluctuates near the lowest output power (13-18 kW) most of the time. When PEMFC doesn’t provide energy, its power gradually decreases to 0. Therefore, the idle running time of the fuel cell is also relatively long.

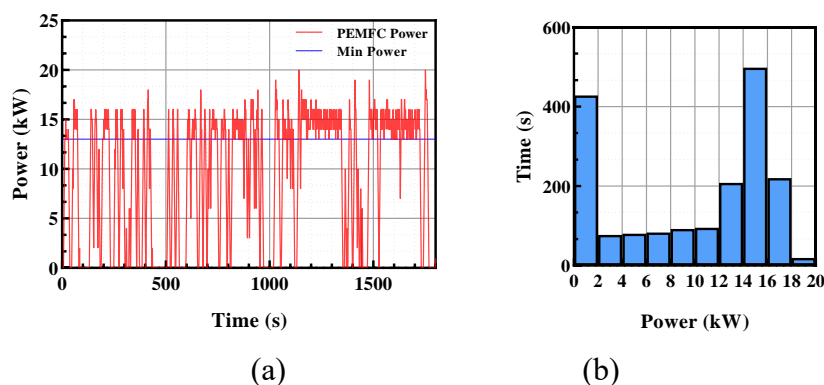


Figure 2. (a) PEMFC’s Power-t curve using DP EMS and (b) histogram of designed profile.

2.2. Design of durability experiment

MEA used in this paper was produced by Wuhan WUT New Energy Co., with an active area of 50 cm². PEMFC was activated using parameters in Table 2. It was activated at the voltage of 0.6 V, 0.5 V, 0.4 V for 1 hour until its performance didn’t rise. After activation, the performance of fresh PEMFC was measured. Then designed PEMFC engine power profile in Fig. 2a) was transformed into a 50 cm² current vs. time curve, and the activated single PEMFC conducted durability experiments by following the transformed curve for 100 cycles. During the experiments, the pressures of anode and cathode were set to 0.8 bar. Stoichiometry of anode and cathode were 1.5, 2.8, respectively. Relative humidity RH of both sides was 75%. The PEMFC’s operating temperature was kept at 80 °C. Polarization curve, EIS, localized EIS tests were conducted after the profile was cycled 20, 40, 60, 80, 100 times.

Table 2. operating conditions of PEMFC.

Parameters	Pressure(bar)	Anode Stoich.	Cathode Stoich.	Temp.(°C)	RH (%)	ActiveArea (cm ²)
Value	0.8	1.5	2.8	80	75	50

The flow field of anode PEMFC was three-channel serpentine. The cathode flow field was four-channel serpentine. A cylinder clamped the whole fuel cell with a pressure of 0.9 MPa. Greenlight G20 platform was used to control gas flow rates, relative humidity, gas pressures, fuel cell current, and monitor voltage value. Gamry reference 3000 was used to conduct Electrochemical Impedance

Spectroscopy (EIS). The anode flow fields and gas inlet/outlet positions are shown in Fig. 3a). There were 6 segments (Seg 1-6) that can do Localized EIS, as highlighted in Fig. 3a).

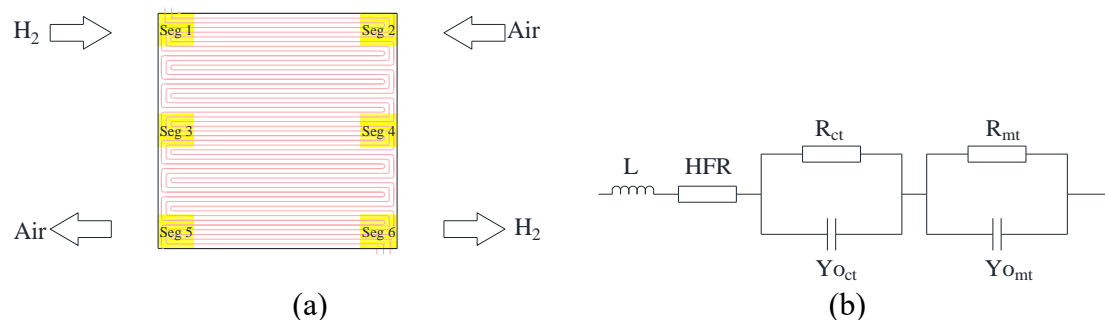


Figure 3. (a) gas inlet/outlet positions and 6 segments that performed Localized EIS; (b) equivalent circuit model that used in EIS and Localized EIS.

Polarization curve was measured at current density of 0, 2, 4, 6, 8, 10, 15, 20, 40, 60, 80, 100, 150, 200, 300, 400, 500, 600, 700, 800, 900, 1000, 1100, 1200, 1300, 1400, 1500, 1600, 1700, 1800, 1900, 2000, 2100, 2200 mA/cm². I-V measurement stopped when the voltage of PEMFC was below 0.3 V. Sweeping frequency of EIS and Localized EIS was set from 10 kHz to 0.1 Hz. The current was set as 30 A for 5 minutes to ensure the PEMFC was at a steady state while measuring EIS and Localized EIS. An Equivalent Circuit Model (ECM) in Fig. 3b) was used to analyze the corresponding results. This ECM was widely used to analyze Nyquist plots of EIS [23]. Operating conditions were the same as Table 2 when conducting the polarization curve, EIS, and Localized EIS measurement.

3. RESULTS AND DISCUSSION

3.1. Performance Degradation

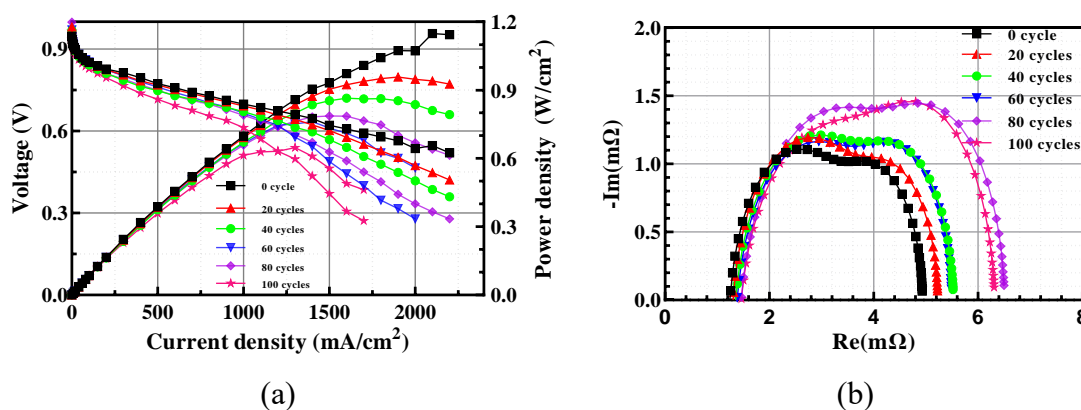


Figure 4. (a) The polarization curves at 80 °C, 75% RH, Anode Stoich. 1.5, Cathode Stoich. 2.8 and (b) The Nyquist curves of PEMFC at 600 mA/cm², 0.8 bar, 80 °C, 75% RH, Anode Stoich. 1.5, Cathode Stoich. 2.8.

I-V curve is displayed in Fig. 4a). The voltage dropped from 0.756 V to 0.694 V at 600 mA/cm² after 100 cycles. The voltage drop rate reached 1240 μ V/h. The peak power dropped from 1.17 W/cm² to 0.65 W/cm². Maximum power decline reached 44.4% after 100 cycles.

Table 3. Fitted data EIS using ECM in Figure 3b).

Cycle	HFR (Ω)	R _{ct} (Ω)	R _{mt} (Ω)	Y _{O_{ct}}	Y _{O_{mt}}	α_{ct}	α_{mt}
0	1.16E-03	1.46E-03	2.32E-03	39.07	3.787	1	0.8992
20	1.22E-03	1.41E-03	2.61E-03	41.21	3.711	1	0.8801
40	1.22E-03	1.59E-03	2.72E-03	36.13	4.316	1	0.8479
60	1.27E-03	1.66E-03	2.57E-03	36.05	4.388	1	0.854
80	1.30E-03	2.00E-03	3.21E-03	31.12	4.417	1	0.8248
100	1.30E-03	2.05E-03	2.97E-03	24.99	4.985	1	0.7968

Compared with other Accelerated Stress Tests, the performance decline was still very rapid [24,25]. Although the current change rate of PEMFC wasn't large under the DP strategy (maximum change rate 47 mA/cm²/s), the fuel cell ran at high potentials for a relatively long time. At high potential, fewer reactants were consumed. Driving by the concentration gradient, the reaction gas might penetrate the proton exchange membrane, generate free radicals, which caused damage to the Proton Exchange Membrane (PEM) and the Catalytic Layer (CL). Proton transportability of the proton exchange membrane declined, the three-phase interfaces at CL decreased, resulting in fast performance deterioration of the PEMFC. Besides, the current fluctuated around 15 A when providing power. The change of current could also lead to a quick decline of PEMFC.

The single cell's EIS results are shown in Fig. 4b). Fitted data are listed in Table 3. It could be seen that as the number of cycles increased, the intersection of the impedance spectrum and the real axis gradually shifted to the right, and the arcs of the curve gradually got larger. Therefore, the internal structure of the fuel cell had been gradually destroyed during the operation.

The high frequency resistance (HFR) of the fuel cell gradually increased. HFR was related to the proton transport ability of the proton exchange membrane. The membrane's proton transport ability declined when HFR increased, indicating that the PEM membrane was corroded under this working condition. The low frequency points represented the process with a large time constant. Therefore, the low-frequency arc represented the mass transfer capacity of the fuel cell, including the resistance of the reactant gas to the reaction site and the flooding phenomenon due to the discharge of water [26]. Larger mass transfer arcs indicated that the reactants/products transport channels of PEMFC were corroded. Materials that helped improve mass transfer, such as the hydrophobic material Polytetrafluoroethylene (PTFE) on GDL, were corrupted. The loss of this component might cause the drainage capacity to decrease. The high-frequency arc represented the charge transfer process of PEMFC, which was associated with the electrons transfer at the electrode/electrolyte interface during half-reaction processes. It depended on the chemical reaction kinetics, electrode surface, and electrode potential. Charge transfer resistance R_{ct} gradually increased, indicating that the fuel cell CL also suffered severe corrosion. The three-phase interfaces decreased, therefore the charge transfer ability reduced during the experiments.

3.2. Localized EIS analyses

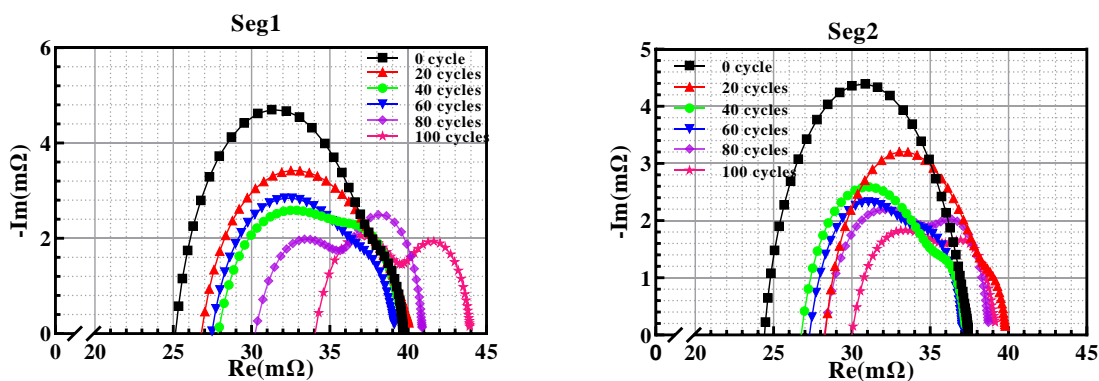


Figure 5. Nyquist plot of Localized EIS of Seg 1-2 at 600 mA/cm², 0.8 bar, 80 °C, 75% RH, Anode Stoich. 1.5, Cathode Stoich. 2.8.

EIS of Seg 1-6 were tested in the experiments. The results showed that different regions had different degradation phenomena.

EIS results of Seg 1-2 are shown in Fig. 5. The two segments were close to the gas inlet area of PEMFC. The gas humidity and temperature in these areas were the closest to the set values, and the gas concentrations were the highest compared to other sites.

From the Nyquist curves of the two regions, it could be seen that the HFRs of the gas inlet region gradually increased. That meant the proton transport ability in the two regions declined. Proton exchange membrane had suffered severe corrosion. Among these two regions, HFR of Seg 1 had the most apparent upward trend, with its high frequency impedance rising from 24.2 to 32.6 mΩ. HFR of Seg 2 had the slowest rising tendency, only increased from 23.7 to 27.8 mΩ. Seg 1 was the area closest to the hydrogen inlet, and Seg 2 the nearest to the air inlet. Therefore, high hydrogen concentration might speed up the degradation of the membrane. Decay mechanisms of PEM can be divided into three categories [27]: mechanical, thermal, and chemical/electrochemical damage. Mechanical damage includes the occurrence of cracks, pinholes, and other damages in the PEM, which may cause direct contact with hydrogen and air. Thermal damage refers to the membrane being decomposed due to high temperature. The decrease of membrane proton transfer ability might due to the formation of Pt bands in the membrane [28,29]. Pt could be oxidized to PtO or PtO₂ by the cathode excess oxygen, and then was dissolved in water in the form of Pt²⁺ or Pt⁴⁺. The Pt ion migrated from the cathode to the membrane, reacted with anode hydrogen, and was reduced to Pt particles. The Pt particles were then re-deposited in the form of Pt crystals. The Pt band hinders the transmission of PEM protons. Since the hydrogen concentration in the gas inlet area is higher, it was more likely to permeate into the membrane and participated in the reduction reaction of Pt. Therefore, the HFR in the gas inlet area showed an upward trend.

The charge transfer resistance R_{ct} of Seg 1-2 also tended to increase, as shown in Fig. 6a). This might because the CL of MEA was corroded and damaged during driving conditions. R_{ct} represents the resistance of charge transfer at the electrode/electrolyte interface. The decreased number of three-phase

interfaces in CL could increase the resistance of charge transfer. In the two segments, the R_{ct} at the air inlet increased was the smallest, which might because the loss of the catalytic layer was mainly at the cathode, and the high air concentration was suitable for the operation of the fuel cell. So the cathode CL loss near the air inlet was small.

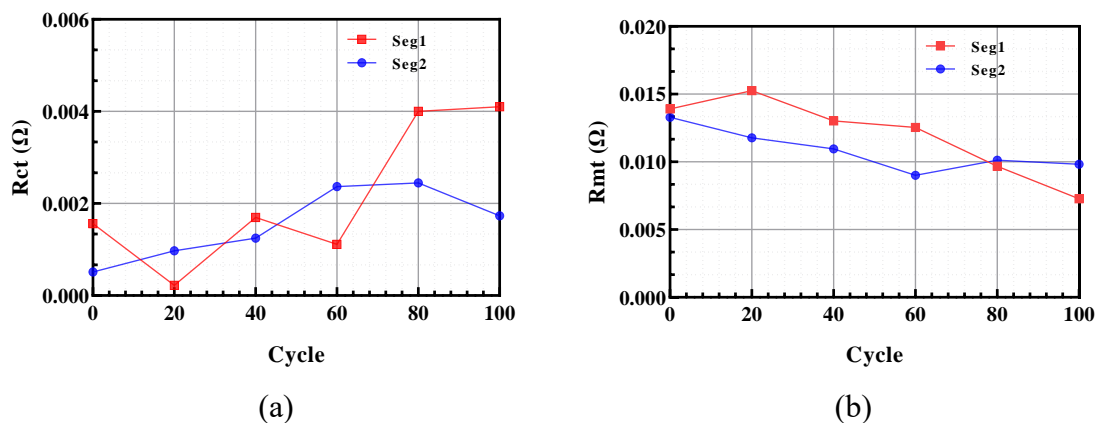


Figure 6. (a) R_{ct} and (b) R_{mt} of Seg 1-2 using ECM in Fig. 3(b).

The low-frequency part of the AC impedance spectrum represented the process that had a large time constant, which was the slowest process in the fuel cell reaction process. It was generally the mass transmission part. This part was related to the flooding phenomenon [26,30]. Accumulated water could block the micro gas transmission channel and thus prevented the reactants from reaching the reaction sites. Fig. 6(b) shows the variation of R_{mt} with the number of cycles. The overall mass transfer resistance had a slightly downward trend, indicating that the Seg 1-2 region's mass transfer became better. This might because Seg 1-2 were near the gas inlet, most of the hydrogen and oxygen did not participate in the electrochemical reaction. Therefore, Seg 1-2 produced less water. The flooding phenomenon wasn't obvious. Besides, the gas concentration were the highest at Seg 1-2, and the mass transmission restriction was the least. Therefore, mass transportation in Seg 1-2 was basically not affected by the corrosion.

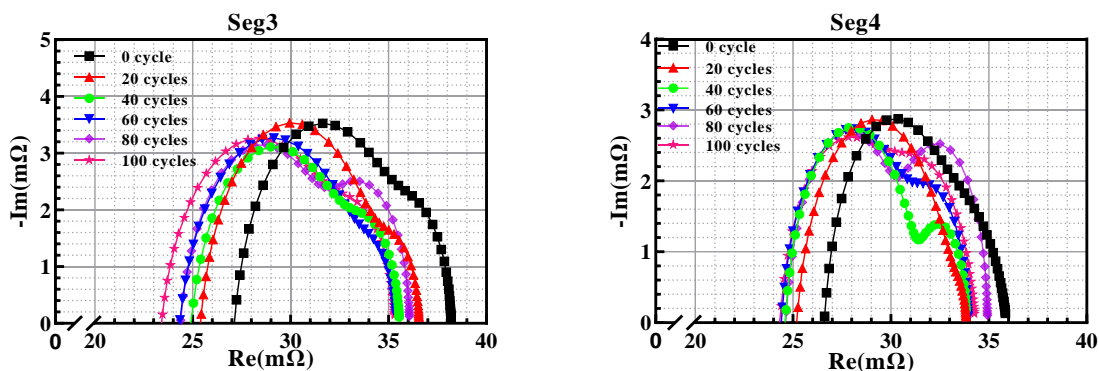


Figure 7. Nyquist plot of Localized EIS of Seg 3-4 at 600 mA/cm^2 , 0.8 bar, $80 \text{ }^\circ\text{C}$, 75% RH, Anode Stoich. 1.5, Cathode Stoich. 2.8.

Seg 3-4 was the middle area of the MEA. The gas flow rates in these areas were more stable than that of the inlet, and the gas concentration was higher than that of the outlet. Therefore, the middle region had good performance. The Localized EIS results are shown in Fig. 7.

The HFRs of Seg 3-4 had slight downward trends, indicating that the proton transmission ability of PEM slightly improved. This phenomenon might be due to two reasons: First, the formation of Pt bands that hindered proton transfer in PEM depended on hydrogen penetration to reduce and deposit Pt^{2+} and Pt^{4+} . Compared with the gas inlet area, the hydrogen concentration of Seg 3-4 was lower. A smaller hydrogen concentration gradient could not deposit Pt on the PEM. So the HFR in the middle region was slightly reduced. Second, the gas passed through the flow channel, participated in the reaction, and generated water. The water was discharged along the flow channel, so the air humidity rose along the flow channel. The PEM's proton conductivity was related to the water content of the membrane. High water content could improve the proton transfer ability [31], so the HFR of Seg 3-4 was lower than that of Seg 1-2. High water content was suitable for the operation of PEM. This might inhibit the damage of PEM.

The mass transfer impedance R_{mt} could be extracted from the low frequency arc of the Nyquist plot. Fig. 8 shows that R_{mt} remained basically unchanged during 100 cycles. Compared with Seg 1-2, it can be seen that the concentration of reaction gas affected the degradation of the mass transfer process. The area with high gas concentration had a downward trend of mass transfer impedance. The performance in the middle area of MEA was the best. Its mass transfer capacity was also better than the gas inlet area.

The R_{ct} of Seg 3-4 had a slight upward trend, which was due to the CLs damage when running the fuel cell under the designed DP EMS profile. However, because of the better operation conditions and the stable gas flow in the middle area, The R_{ct} did not show obvious upward trends. Therefore, the CL layer suffered less damage.

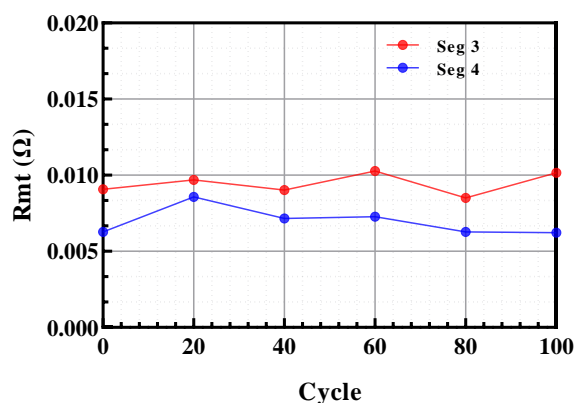


Figure 8. R_{mt} of Seg 3-4 using ECM in Fig. 3(b).

Seg 5-6 belonged to the gas outlet area, where the concentration of H_2 and O_2 was the lowest. Gas humidity should be the highest as water was generated along the flow channel. Therefore, the performance near the gas outlet area was low. The EIS results of Seg 5-6 are shown in Fig. 9. The Nyquist

curve tended to move away from the real axis over time, and the low-frequency arc became more obvious over time.

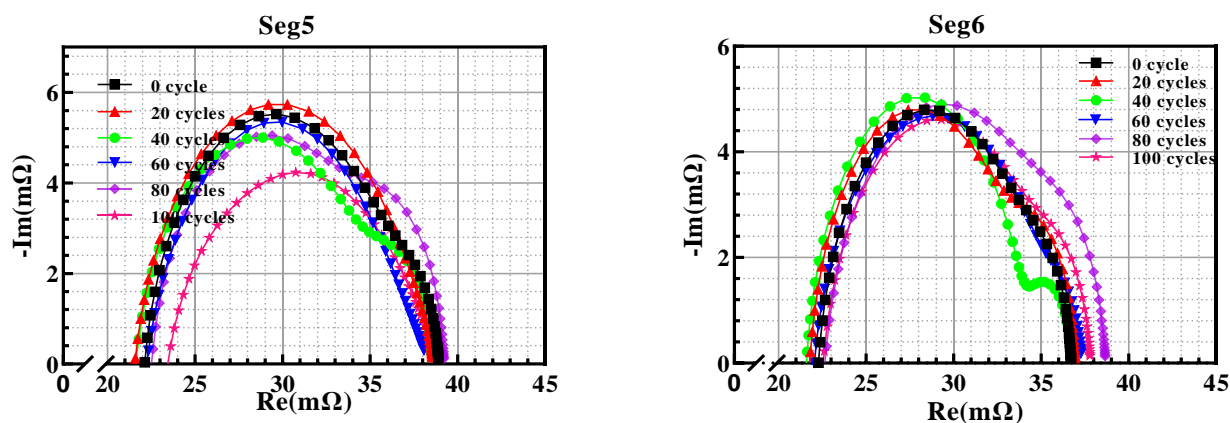


Figure 9. Nyquist plot of Localized EIS of Seg 5-6 at 600 mA/cm², 0.8 bar, 80 °C, 75% RH, Anode Stoich. 1.5, Cathode Stoich. 2.8.

HFR change could be seen shown in Fig. 9. The HFRs of Seg 5-6 were basically unchanged. The maximum increase of HFR in Seg 5-6 was only 2.6 mΩ after 100 cycles. Therefore, the HFR of the PEMFC did not change significantly. This might because higher water content in the gas outlet area made the PEM fully hydrated. Its proton conductivity was basically not affected; besides, the low hydrogen concentration was not enough to reduce and deposit Pt ions on the membrane.

The change of HFR might be related to the high hydrogen concentration and the water content of the membrane. In areas where the membrane's water content was sufficient, HFR was basically not affected by durability cycles. Due to the relatively high hydrogen concentration in the gas inlet area, it was easier to re-deposit the Pt ions on the membrane and damage the performance of the membrane.

4. CONCLUSIONS

The running profile of the PEMFC engine was obtained by using dynamic programming energy management strategy under WLTC. The degradation mechanisms were investigated by running the single 50cm² PEMFC in the designed profile for 100 cycles. The voltage degradation rate reached 1240 μV/h at 600 mA/cm². The proton exchange membrane and the CLs suffered fast corrosion compared with other AST experiments.

Localized EIS of 6 segments were measured to study different areas' degradation phenomena. Change trends of HFR were related to hydrogen concentration and water content of membrane. Proton transfer ability declined at high hydrogen concentration areas as hydrogen might cause Pt reduction and deposition at the PEM. Fully hydrated area of the membrane could provide good proton transfer circumstance and help alleviate PEM degradation. Therefore, Seg 1-2 that closed to gas inlet region had

increased HFR, while other areas' HFR decreased or basically didn't change. Seg 1-2 also had larger HFR compared to other segments. This was because there was not much water produced to fully hydrate PEM in these areas. Therefore, the proton transport ability was worse.

The catalyst layer CL was also corroded. CL could provide reaction sites, flow paths for the supply of reactants and removal of products, and transport electrons and protons. Charge transfer resistance of the PEMFC increased from 1.46 to 2.05 mΩ. This was due to the designed cycle caused the loss of Pt, which inevitably led to the loss of electrochemical surface area (ECSA), and irreversibly reduced the performance of PEMFC. Corrosion of carbon support and ionomer could also decrease reaction sites.

In general, the low-frequency arcs of the AC impedance spectra of Seg 1-6 tended to become larger. The mass transfer capacity of the entire MEA area had a certain degree of decline. Mass transfer was related to the flooding phenomenon. The drainage capacity decreased in the experiments. Reaction gas could not reach the reaction sites smoothly, and the generated water accumulated, which caused the flooding phenomenon to become worse during the experiments. Therefore, the mass transfer arc became larger. At the later stage of durability tests, Seg 1-2 suffered less from the mass transfer. It could be attributed to less water produced and did not accumulate near the gas inlet area.

ACKNOWLEDGEMENT

The authors gratefully acknowledge the financial support by National Natural Science Foundation of China (No. 21978223) and National Key Research and Development Program of China (No. 2017YFB0102803).

References

1. G. Hu, X. Wu, Y. Suo, Y. Xia, Y. Xu, Z. Zhang, *Int. J. Electrochem. Sci.*, 13 (2018) 2080–2089.
2. B. Feng, R. Lin, D. Liu, D. Zhong, *Int. J. Electrochem. Sci.*, 14 (2019) 2175–2186.
3. M.S. Mohy Eldin, A.E. Hashem, T.M. Tamer, A.M. Omer, M.E. Yossuf, M.M. Sabet, *Int. J. Electrochem. Sci.*, 12 (2017) 3840–3858.
4. A. Kneer, J. Jankovic, D. Susac, A. Putz, N. Wagner, M. Sabharwal, M. Secanell, *J. Electrochem. Soc.*, 165 (2018) F3241–F3250.
5. C. Sishitla, G. Koncar, R. Platon, S. Gamburgzev, A.J. Appleby, O.A. Velez, *J. Power Sources*, 71 (1998) 249–255.
6. X. Cheng, L. Chen, C. Peng, Z. Chen, Y. Zhang, Q. Fan, *J. Electrochem. Soc.*, 151 (2004) A48.
7. J. Shan, R. Lin, S. Xia, D. Liu, Q. Zhang, *Int. J. Hydrogen Energy*, 41 (2016) 4239–4250.
8. N. Zhao, Y. Chu, Z. Xie, K. Eggen, F. Girard, Z. Shi, *Fuel Cells*, 20 (2020) 176–184.
9. J. Zhang, C. Song, J. Zhang, *J. Fuel Cell Sci. Technol.*, 8 (2011) 1–5.
10. J. Han, J. Han, S. Yu, *Int. J. Hydrogen Energy*, 45 (2020) 13045–13054.
11. R. Lin, Y.S. Ren, X.W. Lin, Z.H. Jiang, Z. Yang, Y.T. Chang, *Energy*, 123 (2017) 367–377.
12. M. Mayur, S. Strahl, A. Husar, W.G. Bessler, *Int. J. Hydrogen Energy*, 40 (2015) 16466–16476.
13. M. Mayur, M. Gerard, P. Schott, W.G. Bessler, *Energies*, 11 (2018) 1–21.
14. J.C. Kurnia, A.P. Sasmito, T. Shamim, *Appl. Energy*, 206 (2017) 751–764.
15. Y. Hames, K. Kaya, E. Baltacioglu, A. Turksoy, *Int. J. Hydrogen Energy*, 43 (2018) 10810–10821.

16. A.M. Bassam, A.B. Phillips, S.R. Turnock, P.A. Wilson, *Int. J. Hydrogen Energy*, 41 (2016) 22453–22464.
17. Z. Fu, Z. Li, P. Si, F. Tao, *Int. J. Hydrogen Energy*, 44 (2019) 22146–22159.
18. D. Fares, R. Chedid, F. Panik, S. Karaki, R. Jabr, *Int. J. Hydrogen Energy*, 40 (2015) 7777–7790.
19. S. Hou, J. Gao, Y. Zhang, M. Chen, J. Shi, H. Chen, *Int. J. Hydrogen Energy*, 45 (2020) 21858–21872.
20. A. Rezaei, J.B. Burl, B. Zhou, *IEEE Trans. Control Syst. Technol.*, 26 (2018) 2198–2205.
21. D. Liu, R. Lin, B. Feng, L. Han, Y. Zhang, M. Ni, S. Wu, *Appl. Energy*, 254 (2019) 113712.
22. T. Wang, Q. Li, Y. Qiu, L. Yin, L. Liu, W. Chen, *IEEE Trans. Energy Convers.*, 34 (2019) 952–963.
23. M. Zhiani, S. Majidi, *Int. J. Hydrogen Energy*, 38 (2013) 9819–9825.
24. Y. Jeon, S.M. Juon, H. Hwang, J. Park, Y.G. Shul, *Electrochim. Acta*, 148 (2014) 15–25.
25. Y. Li, C.Y. Wang, *J. Electrochem. Soc.*, 164 (2017) F171–F179.
26. Q. Meyer, I. Pivac, F. Barbir, C. Zhao, *J. Power Sources*, 470 (2020) 228285.
27. J. Zhao, X. Li, *Energy Convers. Manag.*, 199 (2019) 112022.
28. T. Søndergaard, L.N. Cleemann, L. Zhong, H. Becker, T. Steenberg, H.A. Hjuler, L. Seerup, Q. Li, J.O. Jensen, *Electrocatalysis*, 9 (2018) 302–313.
29. S.V. Venkatesan, M. Dutta, E. Kjeang, *Electrochem. Commun.*, 72 (2016) 15–18.
30. T.-C. Jao, T. Sasabe, S. Uemura, T. Yoshida, S. Hirai, *ECS Trans.*, 75 (2016) 179–188.
31. X. He, G. He, A. Zhao, F. Wang, X. Mao, Y. Yin, L. Cao, B. Zhang, H. Wu, Z. Jiang, *ACS Appl. Mater. Interfaces*, 9 (2017) 27676–27687.